Proc. R. Soc. Lond. A **398**, 117–140 (1985)
Printed in Great Britain

A numerical study of oblique shock-wave reflections with experimental comparisons

BY H. M. GLAZ[1], P. COLELLA[2], I. I. GLASS[3] AND R. L. DESCHAMBAULT[3]

[1] *Applied Mathematics Branch, Naval Surface Weapons Centre, White Oak, Silver Spring, Maryland* 20910, *U.S.A.*
[2] *Mathematics Department, Lawrence Berkeley Laboratory, Berkeley, California* 94720, *U.S.A.*
[3] *Institute for Aerospace Studies, University of Toronto, Toronto, Canada*

(*Communicated by Sir James Lighthill, F.R.S. – Received* 13 *July* 1984)

A direct comparison is made for several occurrences of oblique shock-wave reflections between interferometric results obtained at the University of Toronto Institute for Aerospace Studies (UTIAS) 10 cm × 18 cm hypervelocity shock tube and numerical results obtained by using a current computational method for solving the Euler equations. Very good qualitative agreement is obtained for equilibrium and frozen flow fields except in small regions where the experiments were dominated by viscous flow. The quantitative agreement is very close in some cases but can be out by 10–15 % in cases with non-equilibrium flow or viscous structures or both. Additional parametrized sequences of calculations are presented to assess the utility of the present numerical method in constructing the various reflection–transition lines for perfect inviscid flows in the shock-wave Mach number, wedge-angle (M_s, θ_w)-plane, and the validity of the 'boundary-layer defect' theory.

1. INTRODUCTION

Over the past several years, substantial advances have been made in the numerical analysis of hyperbolic equations of motion, especially the equations of non-stationary gas dynamics. It is now possible to apply routinely the resulting computer codes on problems that involve complex physical phenomena such as flows with multiple shock waves and slipstreams.

Several questions arise from such work. First, how accurate are the numerical results in reproducing solutions of the Euler equations? In particular, to what extent does the truncation error inherent in a numerical method alter the system of equations being solved? For example, large amounts of artificial viscosity can effectively produce a solution to a parabolic approximation of the Euler equations but not to the Navier–Stokes equations and completely miss the fine structure of wave interactions. Secondly, how well do such results compare with experimental data (which deal with real flows, including viscous effects), if such data are available?

Reliable numerical results are needed for a wide variety of non-stationary compressible-flow problems in shock-wave dynamics, explosion–implosion dynamics

and elsewhere; in some cases, there are virtually no experimental data available for analysis. This creates the requirement for a benchmark problem that contains sufficiently complex nonlinear wave interactions to truly validate a computer code and yet is amenable to accurate experimental measurement. The problem of non-stationary oblique shock-wave reflections from a compressive corner in various gases is currently the strongest candidate for this role. The complex wave structure in the Mach-stem region of such flow fields closely resembles the flow-field phenomenology in typical applications (e.g. a spherical explosion reflecting off an ideal surface). Over the past five years, extensive experimental and analytical data were obtained for these problems (Ben-Dor & Glass 1979, 1980; Ando & Glass 1981; Lee & Glass 1984; Shirouzu & Glass 1982; Deschambault & Glass 1983; Deschambault 1984; Hu & Glass 1985; Hu 1985; Hu & Shirouzu 1985; Wheeler & Glass 1985; Wheeler 1985). Additionally, analytic and experimental work has been performed in this area since Mach (1878), and especially the work of von Neumann (1943) on shock-wave theory for gases.

In their comparison of experimental and computational results for this problem, Ben-Dor & Glass (1978) and Deschambault & Glass (1983) concluded that advances in numerical technique would be required before numerical results could be viewed with the same confidence as experimental data. In particular, they found that computer codes were able to obtain correctly the overall reflection pattern but gave poor agreement with interferometric data concerning the detailed structure of the isopycnics (lines of constant density) of the disturbed flow field behind the reflected shock. Many of these computational results were under-resolved as a result of the constraints of the computer technology existing at that time, while the results presented here are fully resolved because they were obtained with an updated low-diffusion scheme on a modern computer (CRAY I), taking full advantage of the computer's vector processor. The main object of this paper is to change this assessment and place the numerical analysis of perfect inviscid compressible flow on an equal footing with experimental methods. The present study will demonstrate this by comparison of the numerical with the experimental results for argon and air.

Such comparisons are complicated by the fact that the flow fields under investigation are not ideal, because of the following phenomena. A boundary layer is induced behind the shock-wave system (figure 1) on the wedge surface. This not only alters the interaction of the slipstreams (S, S′) with the wall but the transition boundary between regular and Mach reflection (Hornung & Taylor 1982). The slipstream is not an ideal contact surface between thermodynamically different states; it spreads and thickens and undergoes transition from a laminar to a turbulent state. In addition, the second shock wave (or Machstem), M′, in double-Mach reflection is non-uniform in strength from the second triple point, T′, to the first slipstream, S, (figure 1). The interaction between this shock wave and the slipstream is not well understood either. The shock becomes a compression wave as it interacts with the slipstream, which remains stable despite the pressure gradient imposed on it. No reflected expansion waves are observed that might neutralize this gradient as in a steady supersonic jet outflow. Finally, the perfect

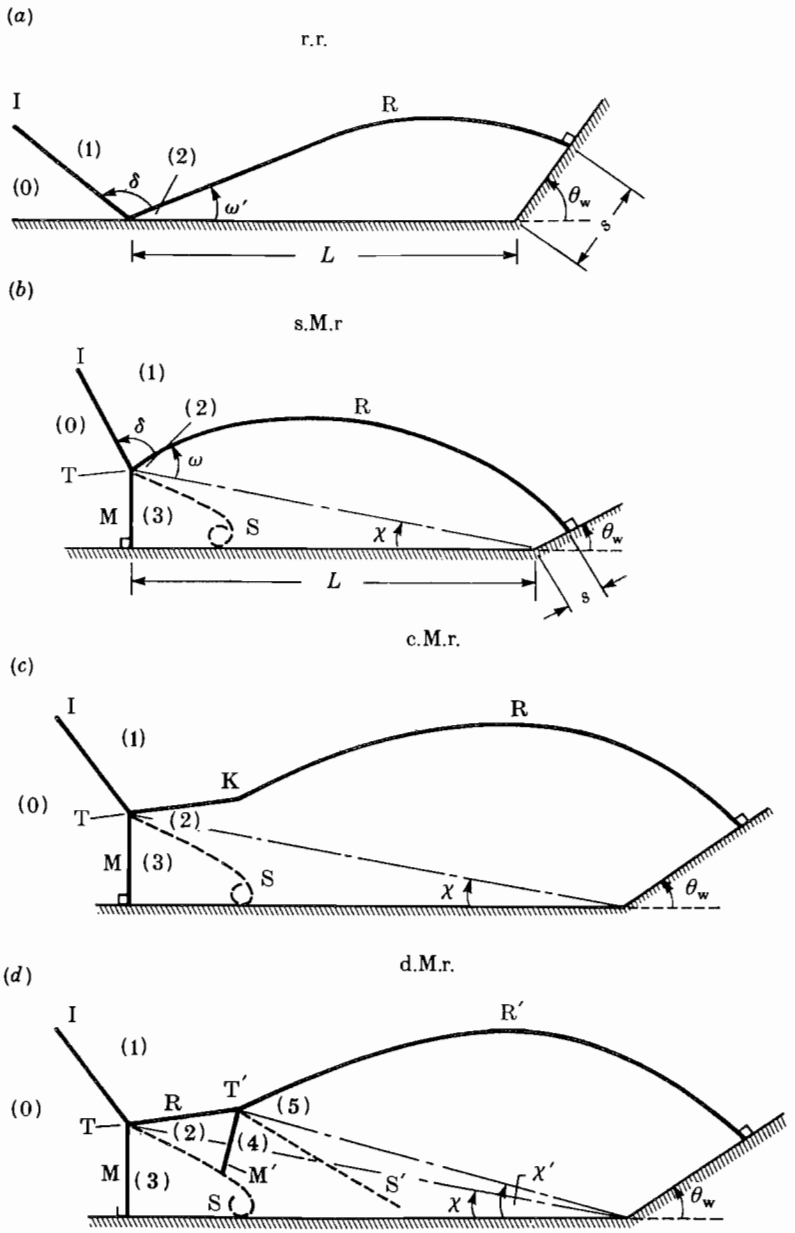

FIGURE 1. Schematic diagrams of types of oblique shock-wave reflections; (*a*) r.r.; (*b*) s.M.r.; (*c*) c.M.r.; (*d*) d.M.r.; also definitions of L and s.

(frozen) flows in air become excited and may be in non-equilibrium or equilibrium states. This complicates the numerical analyses, which now require complex equations of state for equilibrium flows or rate equations for the excitation of the internal degrees of freedom such as dissociation and ionization for non-equilibrium flows at high initial shock-wave Mach numbers.

2. Oblique shock-wave reflections

The four types of pseudo-stationary oblique shock-wave reflection patterns are shown in figure 1 and consist of (*a*) regular reflection (r.r.), (*b*) single Mach reflection (s.M.r), (*c*) complex Mach reflection (c.M.r.) and (*d*) double Mach reflection (d.M.r.). Figure 1 illustrates the definitions of wedge angle θ_w, triple-point trajectory angles, χ, χ', various shock waves I, R, R′, M, M′, slip surfaces S, S′ and the flow regions 1–5 produced by r.r., s.M.r., c.M.r. and d.M.r. reflections. The angle δ between the incident I and reflected R shock waves is also shown as well as the angle ω' between R and the wall or R and the triple-point trajectory χ. The bow shock stand-off distance s, and the length L, between the wedge corner and the reflection point or Mach stem are also indicated. Such quantities can be measured experimentally or predicted numerically and provide important information on the state of the gas whether frozen, non-equilibrium or equilibrium (Shirouzu & Glass 1982; Hu 1985; Hu & Glass 1985).

If real-gas and viscous effects can be ignored, the problem has no intrinsic length-scale, suggesting the use of the self-similar or pseudo-stationary coordinate system $(\xi, \eta) = ((x-x_0)/(t-t_0), (y-y_0)/(t-t_0))$ where (x_0, y_0) are the coordinates of the wedge corner and t_0 is the time at which the incident shock wave reaches the corner. Jones *et al.* (1951) show that the non-stationary Euler equations referred to in this coordinate system transform into the steady Euler equations with the addition of source terms. We note that the ratio s/L is constant for given initial conditions, for self-similar solutions of the non-stationary equations (Li & Glass 1985), just as s is constant for steady supersonic flow. In this and other ways a change to pseudo-stationary coordinates is very useful in the analysis of these flow fields and will be used in this study.

In particular, the type of reflection pattern is a function of the incident shock-wave Mach number M_s, the wedge angle θ_w, and the gas equation of state. The transition boundaries in the (M_s, θ_w)-plane for oblique shock-wave reflection are reproduced from Lee & Glass (1982) in figure 2 for real air and a polytropic equation of state with $\gamma = 1.40$. The analogous figure for argon ($\gamma = \frac{5}{3}$) may be found in this reference. The construction of the transition lines is based on various (heuristic) transition criteria and the numerical calculation of the jump conditions at reflection and triple points. These criteria, which have been the subject of extensive investigation in the literature, are summarized in Lee & Glass (1984) and Shirouzu & Glass (1982). In §5, the numerical results will be used to partly assess the validity of some of these criteria as well as the overall accuracy of the transition diagram, figure 2.

The fourfold partition of the (M_s, θ_w)-plane illustrated in figure 2 is quite coarse relative to the rich phenomenology present in these flow fields. Some other features that may be similarly partitioned (see Ben-Dor & Glass 1979) are (*a*) whether or not the reflected shock is detached or attached to the wedge corner; (*b*) in the attached case, whether the flow at the corner is subsonic or supersonic; (*c*) for r.r., whether the flow is subsonic or supersonic (in pseudo-stationary coordinates) at the reflection point and (*d*) for s.M.r., c.M.r. and d.M.r., whether or not M 'toes-out' or 'toes-in'.

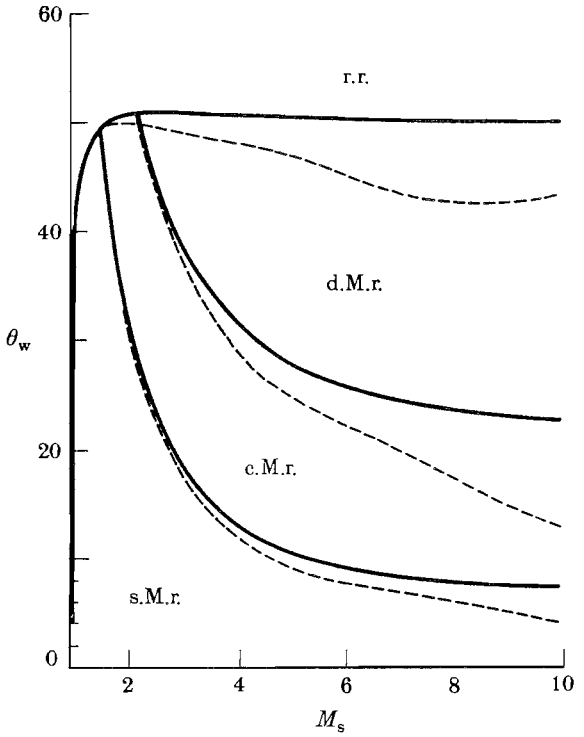

FIGURE 2. Regions of r.r., s.M.r., c.M.r. and d.M.r. and their transition boundaries in the (M_s, θ_w)-plane for perfect (frozen) air solid lines and imperfect (equilibrium) air broken lines, $p_0 = 2.00$ kPa, $T_0 = 300$ K, $\gamma = 1.40$.

A comprehensive study of these issues is beyond the scope of this paper, but they will be discussed as appropriate in the comparison of experimental and numerical results in §5.

3. Experimental techniques

The experiments for this study were performed in the University of Toronto Institute for Aerospace Studies (UTIAS) 10 cm × 18 cm hypervelocity shock tube. Background on the performance and operation of the shock tube can be found in Boyer (1964), with the details of the experiments in Deschambault (1984). The facility includes specialized instrumentation used to record density and pressure in the complex flow fields generated in the present experiments.

The shock tube test section is equipped with large high-quality interferometric windows. To study the density distributions of the flow fields a 23 cm diameter field of view Mach–Zehnder interferometer was employed. The specifications and operating instructions for this instrument can be found in Hall (1954). The interferometer was used in the infinite-fringe mode that allows the direct observation of isopycnics (lines of constant density) in the two-dimensional flow field. The light source employed was a giant pulse ruby laser that enabled the recording of dual

wavelength (694.3 and 347.2 nm) infinite-fringe interferograms, with an exposure time of 30 ns. The test gases used in the present work were argon and medical-grade air.

The reflection patterns were produced by the impingement of a normal shock wave with steel wedges. Both cold-gas (CO_2 driver) and combustion-driver techniques were used to produce the incident shock waves into the test gases used in the present study. For further discussion of the facility and error of measurement associated with the instrumentation see Deschambault (1984) and Glaz *et al.* (1985).

For some of the experimental results presented here, it was necessary to use test gases with very low densities and pressures relative to atmospheric conditions. As a result, vibrational non-equilibrium effects must be taken into account when analysing the corresponding interferograms. We note here that it is easy to check for a relaxation zone behind the incident shock wave because such a zone will produce extra fringes parallel to the shock in the post-shock flow field. Behind the reflected shock wave, the characteristic signature of a relaxing gas is the degree of tangential incidence of the isopycnics and the reflected shock wave.

4. Numerical method

The numerical results presented in this paper have been calculated with a version of the Eulerian second-order Godunov scheme for non-stationary gas dynamics of a type considered by Colella & Woodward (1984). The version of the scheme used here is presented in Colella & Glaz (1982, 1983) including the modifications required for non-polytropic gases.

The method is a finite-difference scheme for systems of hyperbolic conservation laws in one space-like dimension; for multidimensional applications such as the shock-on-wedge problem, we employ operator splitting. Differencing is in conservation form and the numerical fluxes are computed by solving zone interface Riemann problems whose time-centred left and right states are computed from the characteristic form of the equations. This technique leads to second-order accuracy in smooth flow and ensures that the method is centred upstream. In practice, the method is very stable and robust. In the immediate vicinity of a strong shock, some dissipation is required; this has been accomplished by smoothly degrading the scheme to the first-order Godunov scheme in such regions. The degree of degradation is a function of the shock width and strength.

For argon, we have used a perfect (frozen) gas equation of state with $\gamma = \frac{5}{3}$. If the shock-tube test gas was air, the equation of state was chosen to be either a perfect (frozen) gas with $\gamma = \frac{7}{5}$ or the Hansen (1959) real air equation of state as modified by Deschambault (1984) for the present application. The efficient solution of the Riemann problem in the context of our second-order Godunov method for an arbitrary equation of state is treated in Colella & Glaz (1982, 1983). Also, these papers demonstrate that the choice of equation of state has a substantial influence on the quantitative numerical results, as might be expected.

As noted in the preceding section, vibrational non-equilibrium, which is only temperature dependent, can be significant for moderate to high Mach numbers

when the test gas is air (at high Mach numbers dissociation effects are also density dependent); for the argon cases considered here, we expect the gas to remain frozen. The choice of an appropriate equation of state for the air calculations depends mainly on the vibrational relaxation length, l_v, behind the shock waves I, R, M of figure 1. If $l_v \gg l$ (where l is a characteristic flow length arising in the problem), then the gas is frozen and the perfect gas equation of state is correct. If $l \gg l_v$, then the gas is in equilibrium and the Hansen equation of state for real air is used. Finally, if $l_v \approx l$, then neither the frozen nor the equilibrium hypothesis is appropriate, and the flow is said to be in non-equilibrium. We have numerically treated such cases as equilibrium flow fields by using the Hansen equation of state, although the only correct procedure would be to solve an extra partial differential equation representing a rate equation for vibrational relaxation (and for dissociation at high Mach numbers). This decision will be an important issue in our discussion of these cases in §5.

The computational mesh and our problem initialization procedure is illustrated in figure 3. Note that these figures are drawn from right to left to conform with

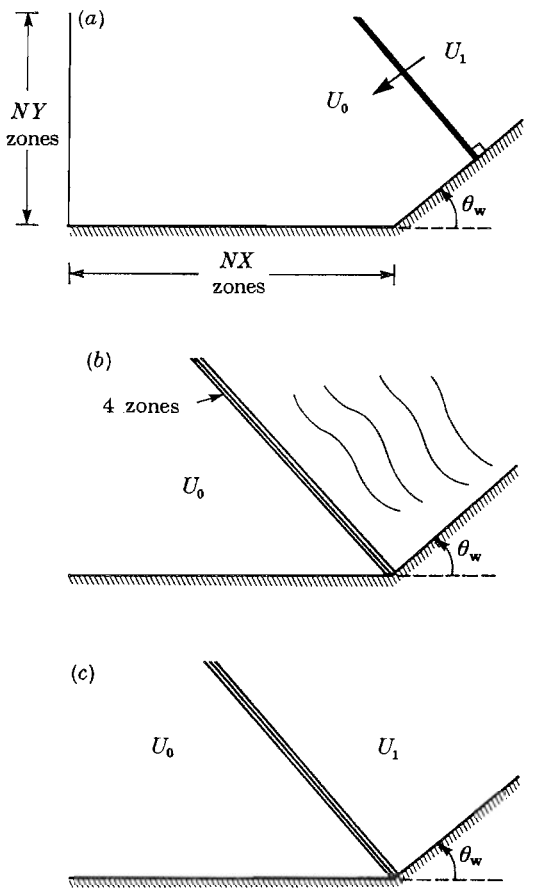

FIGURE 3. Numerical scheme for flow initialization; (*a*) starting procedure; (*b*) shock reaching corner; (*c*) elimination of small disturbances.

the experimental interferograms. We have used a square (i.e. $\Delta x = \Delta y =$ constant) mesh for all of the computations in §5. Because the flow is pseudo-stationary, the choice of Δx is immaterial; however, where a comparison of pressure-gauge records was desirable (see Glaz *et al.* 1985), the total length should be chosen appropriately.

The initial data are taken as $\boldsymbol{U}_0$, M_s where $\boldsymbol{U} = (\rho, p, u, v)^T$ is the state vector and M_s is the initial shock-wave Mach number. From these data and the given equation of state, the post-shock state $\boldsymbol{U}_1$ may be calculated. To initialize the two-dimensional calculation, these data are placed on the grid far upstream (*ca.* 60–75 zones) of the corner, as illustrated in figure 3*a*; interpolation of conserved quantities [i.e. $\boldsymbol{U}^c = (\rho, \rho u, \rho v, \rho E)^T$] is used for zones that straddle the incident shock. However, this is a very poor representation of the numerical shock because any shock-capturing scheme will diffuse a shock wave over two or more zones in the computational mesh. The resulting structure is referred to as a discrete travelling wave (i.e. a mesh function that depends only on $\boldsymbol{x} - \boldsymbol{V}t$, where $\boldsymbol{V}$ is the vector velocity of the wave and equals the shock speed in magnitude for a discrete shock wave). Starting with any initial data (e.g. the one zone $\boldsymbol{U}_0 - \boldsymbol{U}_1$ jump described above) satisfying the Rankine–Hugoniot conditions, the solution will tend as the number of time-steps becomes large towards the appropriate discrete travelling wave, plus other low-amplitude waves that we refer to as 'starting error', with the starting error separating from the travelling wave. For the present application, it is very important to ensure that the starting error is eliminated before the shock wave is allowed to reflect, and we proceed as follows. First, the computer code is allowed to run until the shock wave reaches the corner, and the situation in figure 3*b* is reached. In this figure, the region immediately behind the shock and about 2–3 zones thick is the discrete travelling wave and the small (less than 5 %) relative amplitude disturbances further downstream is the one-time starting error. The computer code then arbitrarily changes the flow field to that illustrated in figure 3*c*, i.e. the discrete travelling wave (arbitrarily set to exactly 4 zones in the computer code) is retained but the starting error is replaced by the post-shock state $\boldsymbol{U}_1$.

At this point, the flow field becomes truly two-dimensional and the computer code is now run without further interruption until the end of the calculation is reached.

The boundary conditions for this problem, which are standard, are discussed in detail in Colella & Glaz (1983). We remark here that our treatment of the intersection of the incident shock with the upper or left-hand boundary or both is not entirely consistent with the discrete travelling wave and leads to the introduction of a low relative amplitude (*ca.* 1 %) wave behind the incident shock at its intersection with the boundary. This wave, which we call a boundary error, may lead to a rather unaesthetic structure in the contour plots and it can impinge on the disturbed flow field behind the reflected shock. Examples will be noted in §5.

All calculations were performed on a CRAY I at Los Alamos National Laboratory, Los Alamos, New Mexico. The computer code was designed to take significant advantage of the machine's vector architecture. Each calculation in §5 required 15–40 min c.p. time with most in the range of 20–30 min. Much of this time is wasted on the extra grid points introduced to eliminate the starting error as well

as grid points outside the reflected shock. Also, a fine mesh is only really needed in the Mach stem region. Thus, an intelligent adaptive mesh structure could reduce these timings substantially.

5. Computational results

A direct comparison of experimental results and numerical calculations is presented in §5.1 for five cases. In §5.2, the results of a parametrized sequence of calculations are presented to demonstrate the capability of our numerical method to compute transition boundaries in the (M_s, θ_w)-plane. An additional sequence is presented to demonstrate (upon comparison with experimental data) the effect of boundary-layer displacement on the r.r. $\rightleftharpoons$ d.M.r. transition.

5.1. *Comparison of experiment with calculation*

The initial conditions for the five cases are listed in table 1 along with the computational mesh (NX, NY) and the equation of state (e.o.s.) selected for each calculation. All four wave configurations are represented in the range of (M_s, θ_w)

Table I. Experimental and numerical initial conditions

case	1	2	3	4	5
gas	argon	air	air	air	air
type	r.r.	s.M.r.	c.M.r.	c.–d.M.r.	d.M.r.
θ_w(°)	60	27	10	20	27
M_s	2.05	2.03	10.37	7.19	8.70
P_0 (kPa)	20.0	33.3	6.7	8.0	4.1
ρ_0 (kg/m^3)	3.23×10^{-1}	3.87×10^{-1}	7.53×10^{-1}	9.29×10^{-2}	4.76×10^{-2}
e.o.s.	$\gamma=\frac{5}{3}$	$\gamma=\frac{7}{5}$	Hansen	Hansen	Hansen
NX	355	350	400	420	440
NY	90	130	140	220	85

considered. The following data are presented for each case: experimental isopycnics, computed isopycnics with the use of the same density levels as were obtained in the experiment, computed isopycnics with the use of thirty contour levels spaced equally between the extreme flow field densities, and a wall-density distribution plot (ρ/ρ_0 against x/L) containing both the numerical and experimental results. Numerically generated contour plots (with thirty equally spaced contour levels) of other flow-field quantities will occasionally be included in the discussion. Of particular interest is the Mach number in pseudo-stationary coordinates, $\tilde{M}$, defined by $\tilde{M}^2(x, y, t) = [(u-\xi)^2+(v-\eta)^2]/a^2$ where a = sound speed. The quantity $\tilde{M}-1$ is plotted so that the zero contour level corresponds to the sonic line in this coordinate system.

Case 1: r.r., $M_s = 2.05$, $\theta_w = 60°$, argon. Comparison of the experimental and numerical isopycnics (figures 4*a*, *b*) show them to be in good agreement with an error of about one fringe at the start of the subsonic region. The wall density distribution (figure 4*d*) disagrees by about the same amount. It may be observed in figure 4*c* that the contour levels curve sharply towards the reflection point just

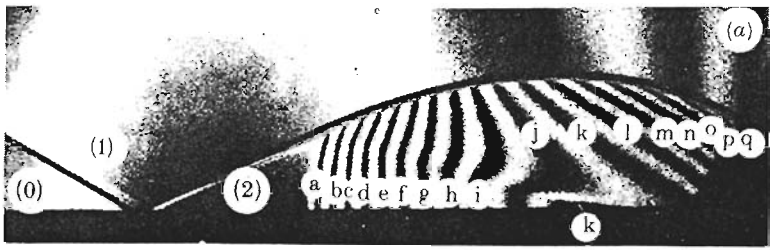

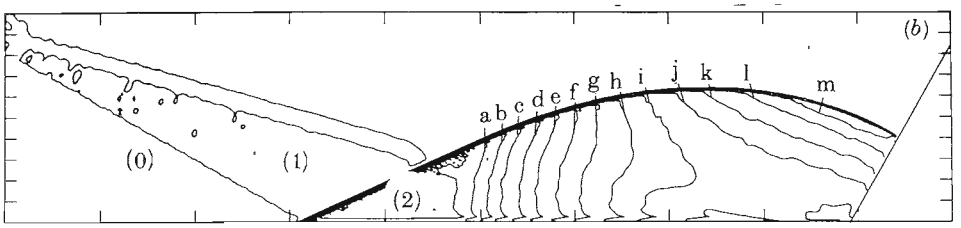

region	ρ/ρ_0	region	ρ/ρ_0	region	ρ/ρ_0
(0)	1.00	*e*	4.06	*l*	3.60
(1)	2.33	*f*	3.99	*m*	3.54
(2)	4.38	*g*	3.93	*n*	3.47
a	4.32	*h*	3.86	*o*	3.41
b	4.25	*i*	3.80	*p*	3.34
c	4.19	*j*	3.73	*q*	3.28
d	4.12	*k*	3.67		

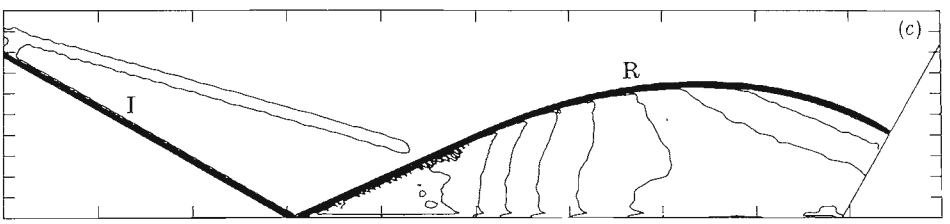

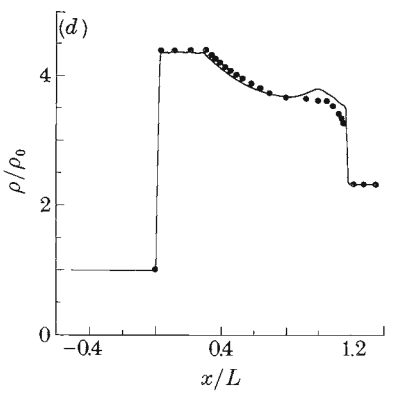

FIGURE 4(*a–d*). For description see facing page.

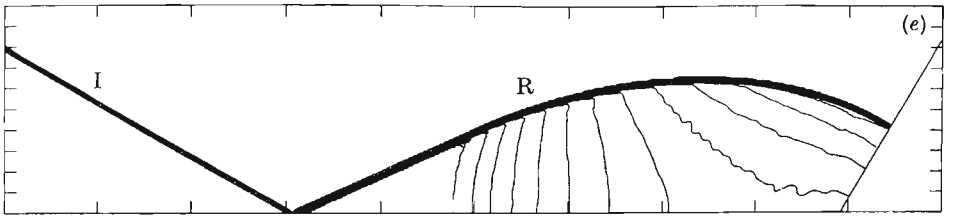

FIGURE 4. Case 1: r.r., $M_s = 2.05$, $\theta_w = 60°$, $p_0 = 20.0$ kPa, $T_0 = 297.6$ K, argon, $\rho_0 = 0.323$ kg/m^3. (*a*) Interferogram and experimental isopycnics; values given in table shown, (*b*) numerically simulated isopycnics shown in (*a*), (*c*) 30 numerical isopycnics, equally spaced between the minimum and maximum flow field densities, (*d*) wall-density distribution; —, computational results; •, experimental data, (*e*) 30 equally spaced numerical isobars.

above the wedge surface, an effect that is not present in the experimental results. This numerical error is referred to as 'wall heating' and is commonly observed in shock capturing calculations as shown, for example, in Noh (1976). Wall heating affects only the density, temperature, etc., and not the pressure (figure 4*e*). It may be seen to account for part of the observed error in this case, including the slight error in the value of the reflected shock wave density ρ_2 on the wall. In addition, the error in the stand-off distance of the bow shock s, relative to the experimental distance from the reflection point P to the corner L, is about 6.2%.

Case 2: s.M.r., $M_s = 2.03$, $\theta_w = 27°$, air. The agreement for this case is extremely good in all respects (figures 5*a–d*). Quantitatively, the isopycnics are out by about one fringe (figures 5*a*, *b*), and the wall-density plot (figure 5*d*) shows similar agreement for its entire length. Note that the contact discontinuity spreads out in the experiment and, consequently, does not roll up as much as in the calculation.

Case 3: c.M.r., $M_s = 10.37$, $\theta_w = 20°$, air. The experimental results (figure 6*a*) show very strong non-equilibrium effects in the disturbed flow field behind the reflected shock, with an almost equilibrium incident shock. The wedge surface does not appear to be straight because of diffraction effects, indicating that the sidewall boundary layer is significant. We get reasonably good qualitative agreement in the isopycnic patterns (figures 6*a*, *c*) although the tangential incidence at the reflected shock in figure 6*a* cannot appear in figure 6*c*. Also, the numerical wall heating is substantial. The quantitative agreement is equally good (figures 6*a*, *b*). In considering the wall-density plot (figure 6*d*), we note that the data points were evaluated assuming frozen triple-point conditions. Also, we measure $\chi = 12.5$–13.25 and 15.3° and the attachment angle = 20–21 and 25.5° for the experiment and calculation, respectively. The latter difference explains the disagreement in figure 6*d* near $x/L = 1.0$. If the vortex roll-up patterns could be lined up and the Hansen equation of state used in evaluating the data, it seems that quite good quantitative agreement could be obtained where x/L is small, despite the wall heating error. The dip in figure 6*d* at $x/L \approx 0.25$ is due to the boundary error.

Case 4: c.M.r.–d.M.r., $M_s = 7.19$, $\theta_w = 20°$, air. The experimental isopycnics (figure 7*a*) show clearly that this flow field is neither frozen nor in equilibrium. Also, the isopycnics leave the reflected shock almost tangentially, which indicates that there are substantial non-equilibrium effects across this wave as well. A more

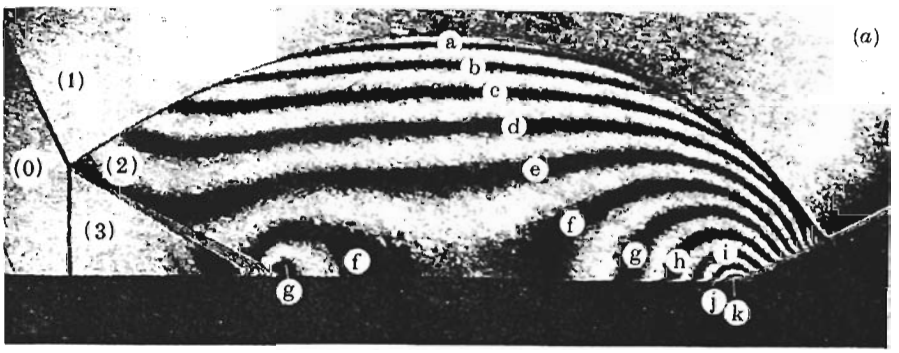

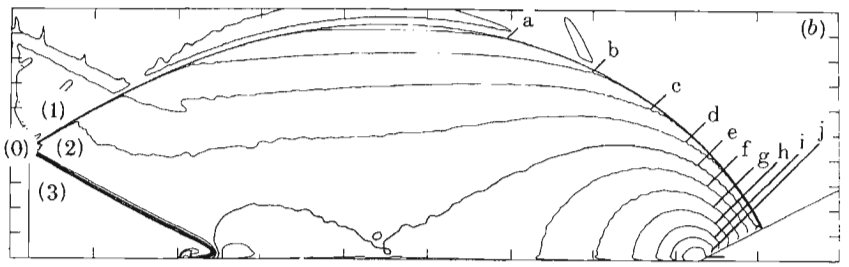

region	ρ/ρ_0	region	ρ/ρ_0	region	ρ/ρ_0
0	1.00	*b*	3.44	*g*	3.83
1	2.71	*c*	3.52	*h*	3.91
2	3.68	*d*	3.60	*i*	3.99
3	3.33	*e*	3.68	*j*	4.06
a	3.36	*f*	3.75	*k*	4.14

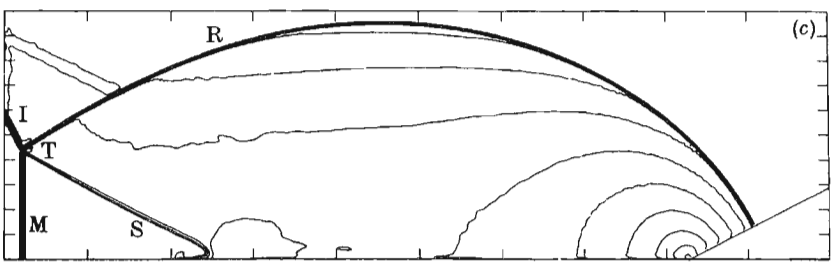

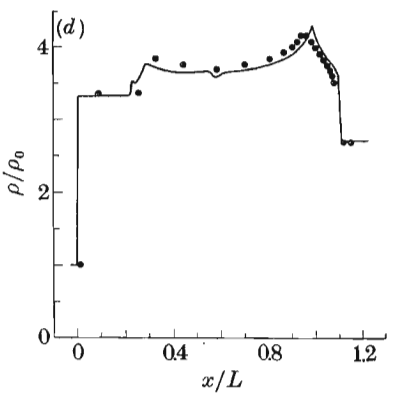

FIGURE 5. Case 2: s.M.r., $M_s = 2.03$, $\theta_w = 27°$, $p_0 = 33.3$ kPa, $T_0 = 299.2$ K, air, $\rho_0 = 0.387$ kg/m^3. (*a*) Interferogram and experimental isopycnics, (*b*) numerically simulated isopycnics shown in (*a*), (*c*) 30 equally spaced numerical isopycnics, (*d*) wall-density distribution; —, computational results; •, experimental data.

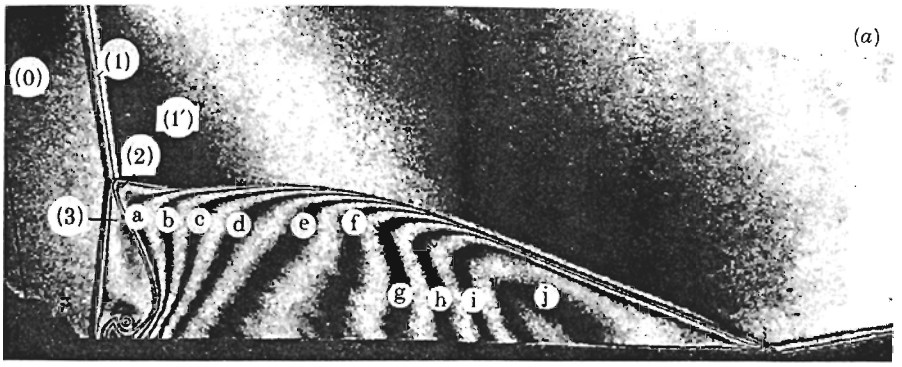

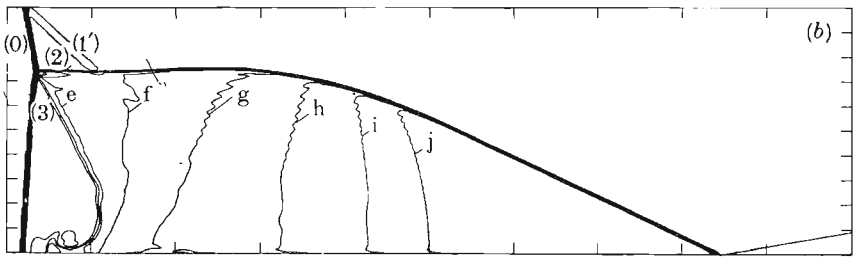

region	ρ/ρ_0	region	ρ/ρ_0	region	ρ/ρ_0
(0)	1.00	*a*	6.70	*f*	8.69
(1)	5.73	*b*	7.10	*g*	9.09
(1′)	6.33	*c*	7.50	*h*	9.49
(2)	6.30	*d*	7.90	*i*	9.89
(3)	5.77	*e*	8.29	*j*	10.29

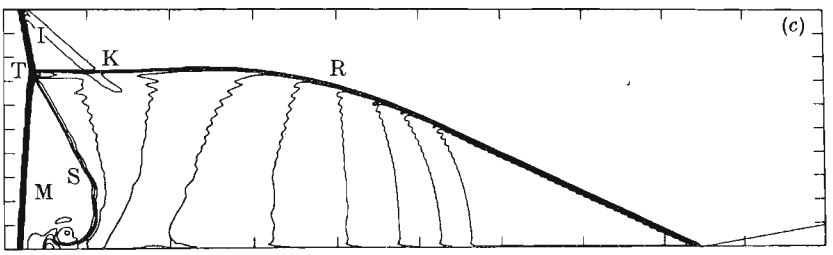

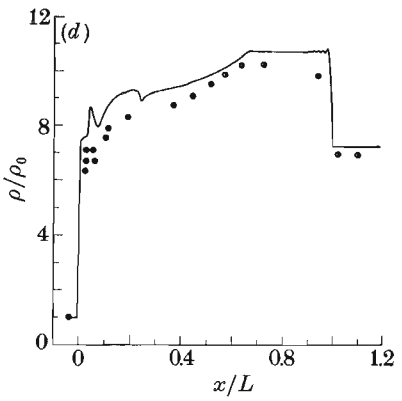

FIGURE 6. Case 3: c.M.r., $M_s = 10.37$, $\theta_w = 10°$, $p_0 = 6.7$ kPa, $T_0 = 299.0$ K, air, $\rho_0 = 0.753$ kg/m^3. (*a*) Interferogram and experimental isopycnics, (*b*) numerically simulated isopycnics shown in (*a*), (*c*) 30 equally spaced isopycnics, (*d*) wall-density distribution; —, computational results; •, experimental data.

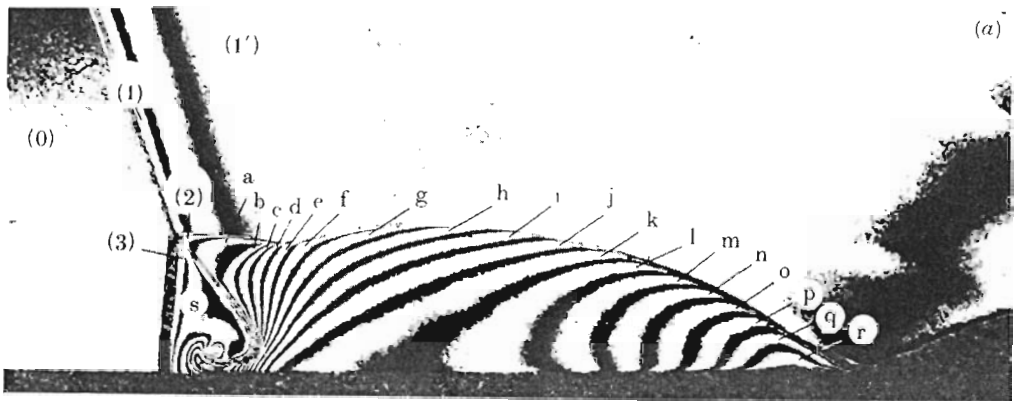

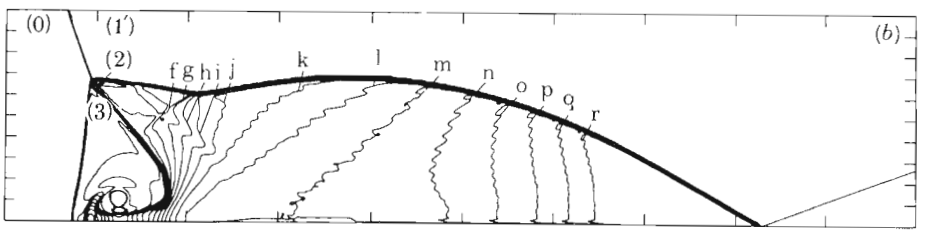

region	ρ/ρ_0	region	ρ/ρ_0	region	ρ/ρ_0
(0)	1.00	*d*	7.94	*l*	10.53
(1)	5.47	*e*	8.27	*m*	10.85
(1′)	6.13	*f*	8.59	*n*	11.18
(2)	6.65	*g*	8.91	*o*	11.50
(3)	5.59	*h*	9.24	*p*	11.82
a	6.97	*i*	9.56	*q*	12.15
b	7.30	*j*	9.88	*r*	12.47
c	7.62	*k*	10.21	*s*	5.91

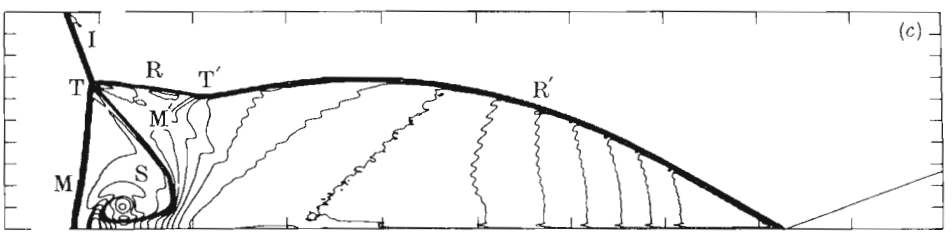

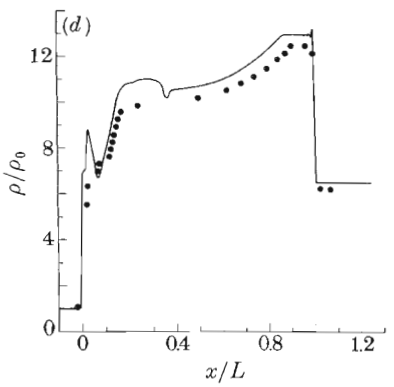

FIGURE 7 (*a–d*). For description see facing page.

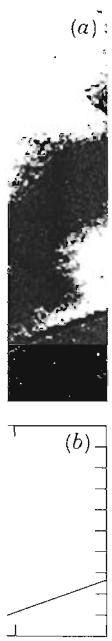

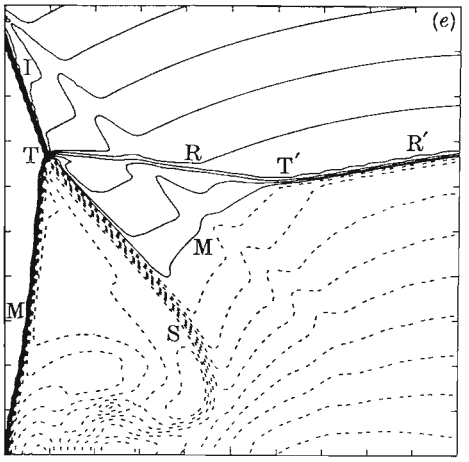

FIGURE 7. Case 4: c.–d.M.r., $M_s = 7.19$, $\theta_w = 20°$, $p_0 = 8.0$ kPa, $T_0 = 298.5$ K, air, $\rho_0 = 0.0929$ kg/m^3. (*a*) Interferogram and experimental isopycnics, (*b*) numerically simulated isopycnics shown in (*a*), (*c*) 30 equally spaced isopycnics, (*d*) wall-density distribution; —, computational results; •, experimental data, (*e*) 30 $\tilde{M}$ contour levels (blowup frame); minimum and maximum M values are relative to the frame.

detailed discussion of equation of state and non-equilibrium effects in the numerical analysis of this case is available in Colella & Glaz (1983). For the equation of state used here, the triple-point angle is in exact agreement. Note that ρ_3/ρ_0 is in very poor agreement (figure 7*d*) because the experimental data reduction used the frozen triple-point conditions. The otherwise excellent agreement for $x/L < 0.15$ is surprising in view of the strong non-equilibrium and viscous effects in this region. The contours, including the vortex pattern, are in excellent qualitative and quantitative agreement (figures 7*a–c*). The attached shock wave at the corner is bifurcated in the experiment (figure 7*a*). The flow there is supersonic in the calculation (figures 7*b*, *c*). The $\tilde{M}$ contours (figure 7*e*) show the sonic line approaching the kink that corresponds to this case lying on the c.M.r.–d.M.r. transition boundary; Lee & Glass (1984) conjecture that this transition occurs when the sonic line reaches the kink. This case is an excellent example of the effects of the computational boundary error on the disturbed flow field (figures 7*b–d*; $x/L \approx 0.35$).

Case 5: d.M.r., $M_s = 8.7$ $\theta_w = 27°$, air. Figure 8*a* exhibits substantial non-equilibrium effects. In particular, $l_v \approx 0.2$ x/L for the incident shock and the isopycnics are at tangential incidence to the reflected shock. Also, the relaxing gas in the Mach stem region has obscured the slipstream and part of the roll-up pattern. Comparison of figures 8*a*, *c* show very good agreement. The roll-up pattern agrees very well, although the slipstream normal to the wall at $x/L \approx 0.02$ and the backward facing shock normal to the wall at $x/L \approx 0.065$ in figure 8*c* are either not resolved or are lost as a result of viscous effects in figure 8*a*. Details of the calculated flowfield in the Mach stem region are presented in figures 8*e–g*. The existence of an extra pseudo-stationary stagnation point where the velocity is zero is noted in figure 8*g*. We have measured $\chi = 9.6$ and 7.0° and R (≡ ratio of

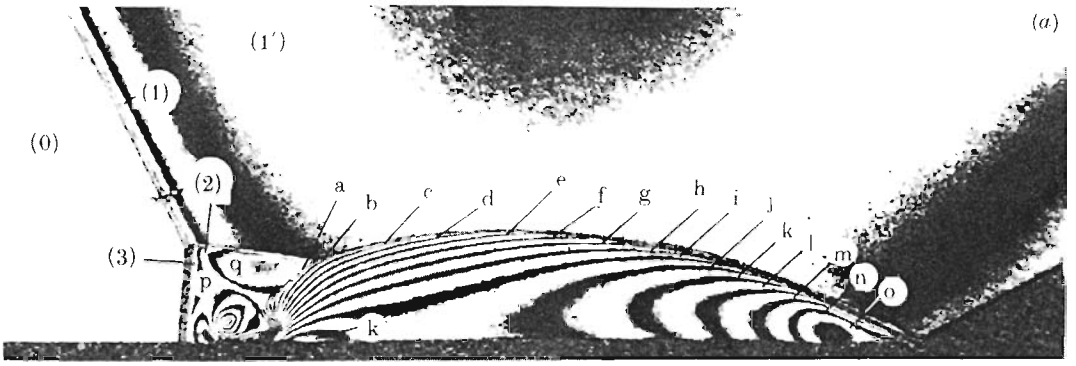

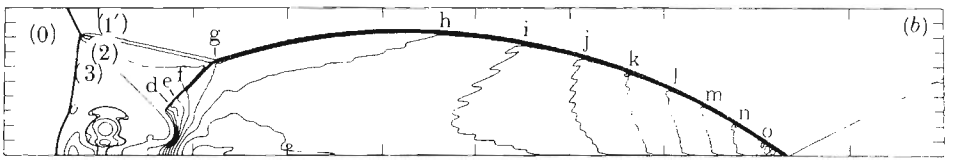

region	ρ/ρ_0	region	ρ/ρ_0	region	ρ/ρ_0
(0)	1.00	d	11.42	k	15.84
(1)	5.63	e	12.05	l	16.47
(1′)	6.89	f	12.68	m	17.10
(2)	7.44	g	13.32	n	17.73
(3)	5.74	h	13.95	o	18.36
a	9.53	i	14.58	p	6.37
b	10.16	j	15.21	q	8.07
c	10.79				

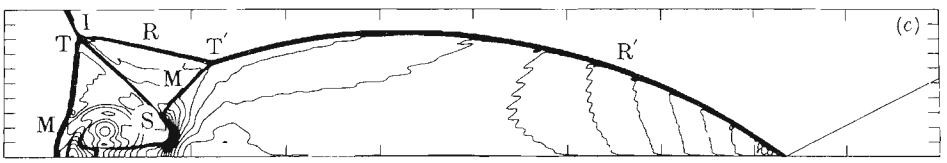

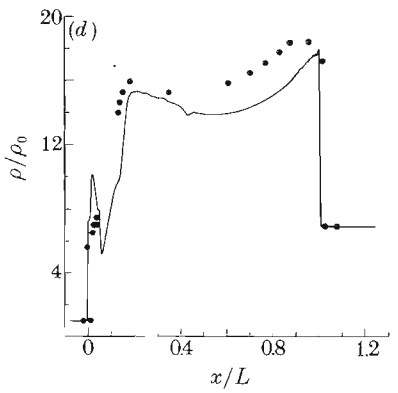

FIGURE 8(*a–d*). For description see facing page.

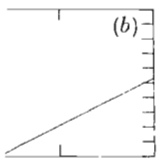

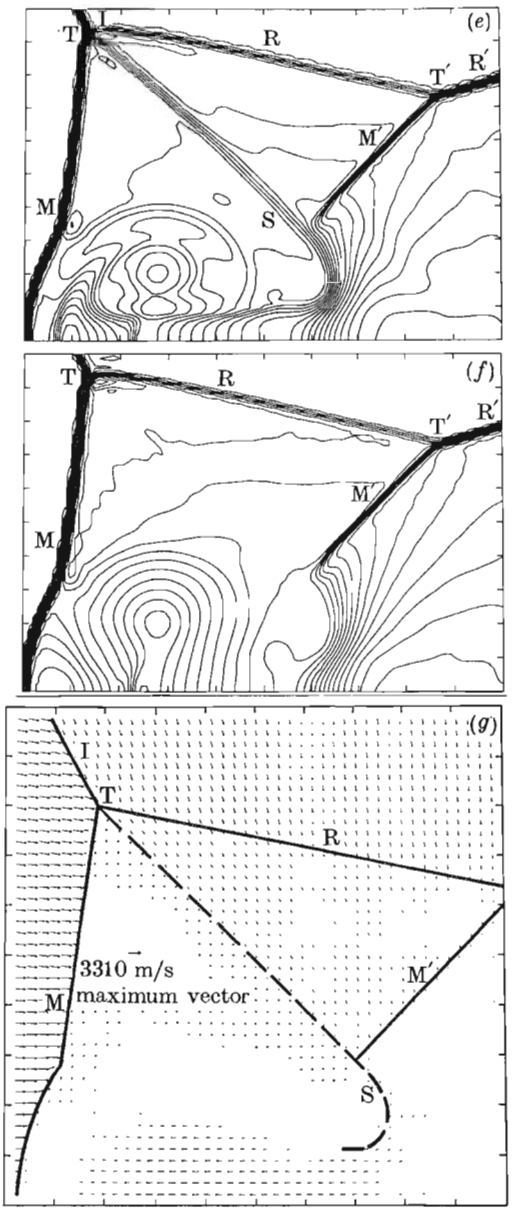

FIGURE 8. Case 5: d.M.r., $M_s = 8.70$, $\theta_w = 27°$, $p_0 = 4.1$ kPa, $T_0 = 299.2$ K, air, $\rho_0 = 0.0476$ kg/m^3. (*a*) Interferogram and experimental isopycnics, (*b*) numerically simulated isopycnics shown in (*a*), (*c*) 30 equally spaced isopycnics, (*d*) wall-density distribution; —, computational results; •, experimental data, (*e*) density contours (blowup frame), (*f*) pressure contours (blowup frame), (*g*) ($\tilde{u}$, $\tilde{v}$)-vector plot (blowup frame plus overlay of wave system).

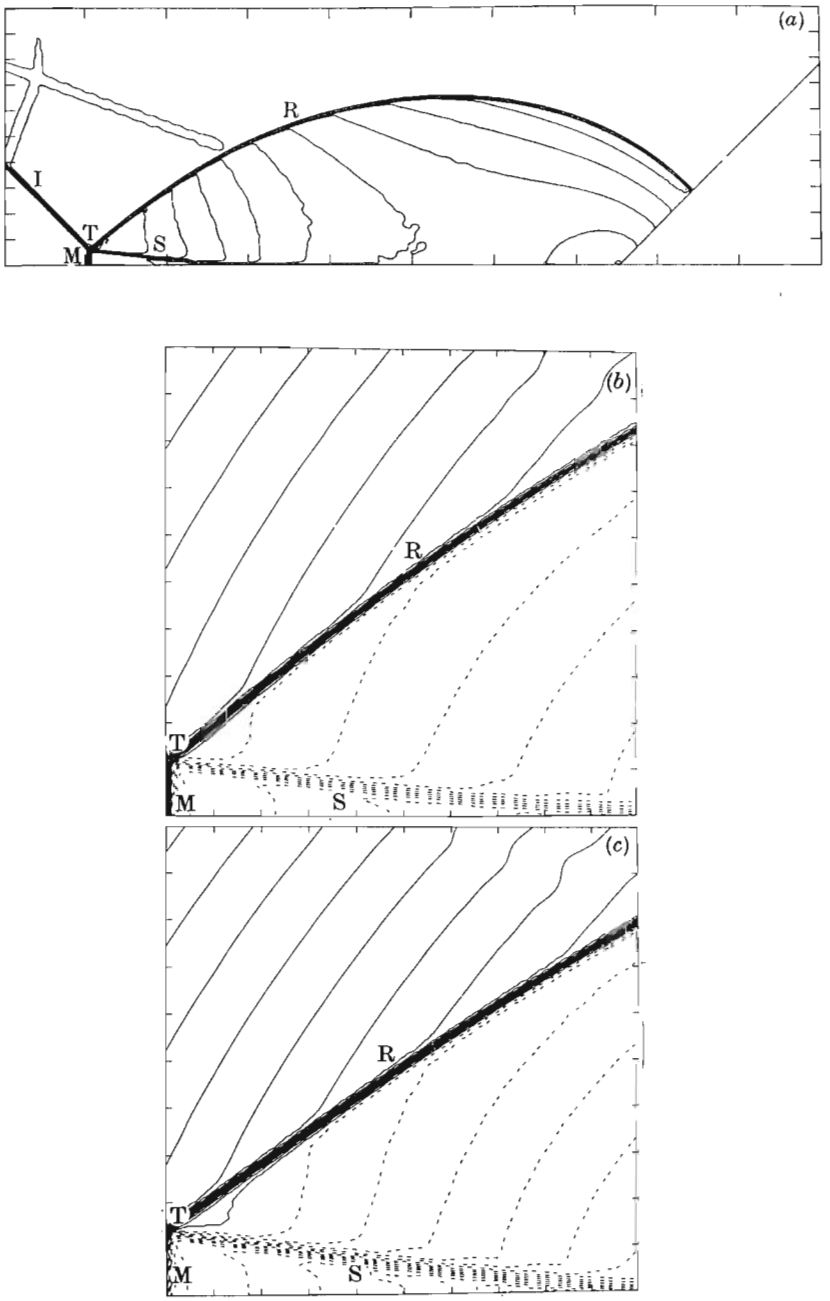

FIGURE 9(*a–c*). For description see facing page.

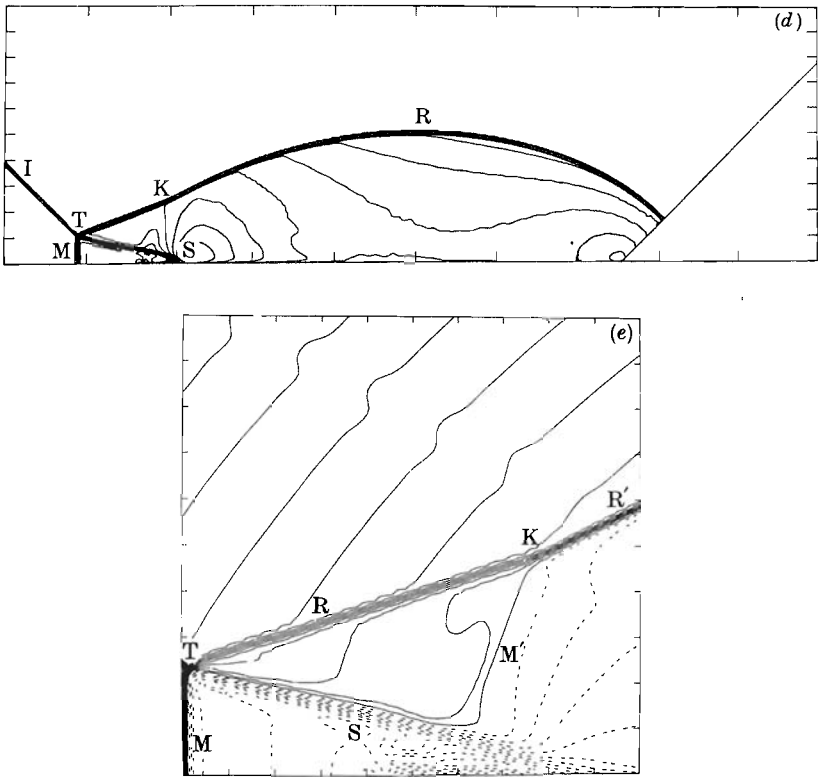

FIGURE 9. Transition sequence for perfect (frozen) air, $\theta_w = 45°$; (*a*) isopycnics, $M_s = 1.70$, $\theta_w = 45°$, (*b*) $\tilde{M}$ blowup for $M_s = 1.70$, showing sonic line interior to the reflected shock, (*c*) $\tilde{M}$ blowup for $M_s = 1.80$, showing region of supersonic flow beneath the reflected shock, (*d*) isopycnics, $M_s = 2.30$, $\theta_w = 45°$, d.M.r., (*e*) blowup showing details of $\tilde{M}$ for case (*d*) above, where sonic line intersects the kink.

the distance between the two triple points and L) = 0.1854 and 0.1769 for the calculation and experiment, respectively. The data points in figure 8*d* near $x/L = 0.0$ were obtained by using the triple-point conditions for $\gamma = 1.40$ and $\chi = 7.0°$. The measured corner attachment angles are 33.5 and 23.0° for the calculation and experiment, respectively. This non-equilibrium effect (which apparently is poorly modelled with the equilibrium Hansen equation of state) explains the disagreement near $x/L = 1.0$ in figure 8*d*. We note that the numerical thermal layer is a large effect for this problem. Overall, real-gas effects have an extensive impact on the flow dynamics for this case and the equilibrium calculation cannot reproduce these effects.

5.2. *Transition sequences*

We have calculated a sequence of cases for perfect air at $\theta_w = 45°$ for $1.3 \leqslant M_s \leqslant 2.6$ in increments of $\Delta M_s = 0.1$. Because of lack of space, only a small portion of the results will be presented here. The full study, as well as the calculations for other line segments in the (M_s, θ_w)-plane are included in Glaz

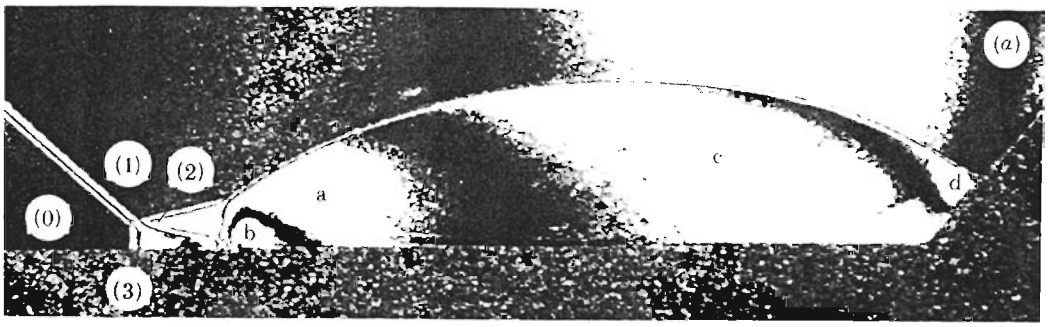

region	ρ/ρ_0	region	ρ/ρ_0
(0)	1.00	a	7.94
(1)	3.78	b	9.19
(2)	6.69	c	6.69
(3)	3.91	d	5.44

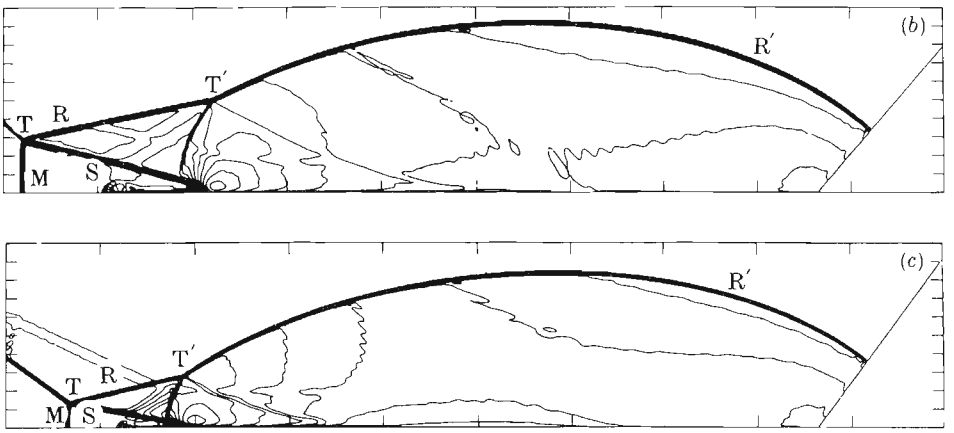

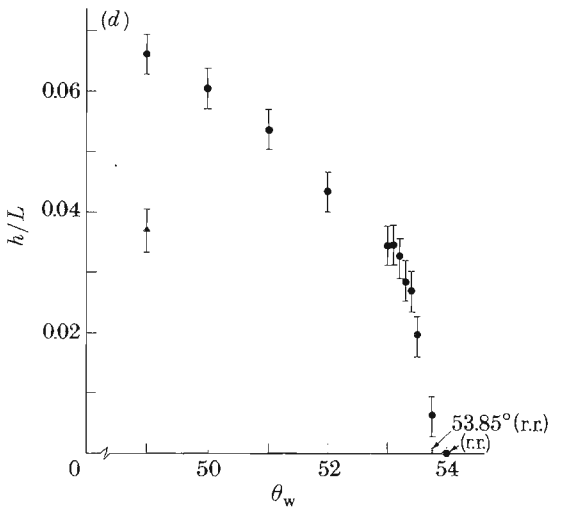

FIGURE 10. Transition sequence for argon, $M_s = 7.1$. (a) Interferogram and experimental isopycnics, $M_s = 7.1$, $\theta_w = 49.0°$, $p_0 = 2.0$ kPa, $T_0 = 296.3$ K, $\rho_0 = 0.0329$ kg/m^3, (b) 30 equally spaced isopycnics, $\theta_w = 49.0°$, (c) 30 equally spaced isopycnics, $\theta_w = 53.2°$, (d) Plot of d.M.r. Mach stem height versus θ_w, extrapolated to zero height for r.r. ($h/L = 0$ for $\theta_w = 53.85°$), $h/L = 0$ for $\theta_w = 54°$ is a numerical result. ▲, experimental point; •, numerical results.

perimental
/m³, (*b*) 30
.2°, (*d*) Plot
h/*L* = 0 for
, numerical

et al. (1985). The purpose of these calculations is to demonstrate the feasibility of using the computer code to construct the inviscid transition lines in the (M_s, θ_w)-plane and to test transition theories based on inviscid arguments.

The contours of constant density for the case where $M_s = 1.70$ are shown in figure 9*a*. The configuration can be seen to be near the s.M.r. $\rightleftharpoons$ c.M.r. boundary, but it is difficult to judge precisely the shape of the reflected shock. Contours of constant self-similar Mach numbers in the vicinity of the triple point are shown for this case and for $M_s = 1.80$ in figure 9*b*, *c*. This sonic line (in pseudo-stationary coordinates) has moved into region 2 for the cases where $M_s = 1.80$; the extent of the supersonic region increases with increasing shock-wave Mach number, $M_s \geqslant 1.80$ (not shown). Assuming that the s.M.r. $\rightleftharpoons$ c.M.r. transition occurs when region 2 becomes supersonic at the triple point (see Lee & Glass 1984), it follows that the $M_s = 1.80$ case is a c.M.r. Similarly, we find that the cases where $1.3 \leqslant M_s \leqslant 1.7$ are s.M.rs, because region 2 is entirely subsonic for these results (not shown). Therefore, the computer code predicts the 45°, perfect gas s.M.r. $\rightleftharpoons$ c.M.r. transition to lie in the range $1.70 \leqslant M_s \leqslant 1.80$. We remark that the analogous calculations for 45°, imperfect air with the Hansen equation of state (not shown) predicts $1.60 \leqslant M_s \leqslant 1.70$ for the same transition. Both results agree reasonably well with figure 2, but the Hansen results are in better agreement. A more precise prediction would simply be a matter of choosing a smaller value of ΔM_s and, perhaps, by using more mesh points in the triple-point region to improve resolution.

The results for the weak d.M.r. case, $M_s = 2.30$, are shown in figure 9*d*, *e*. One theory for the c.M.r. $\rightleftharpoons$ d.M.r. transition (see Lee & Glass 1984) is that the flow at the first triple point should be supersonic with respect to the motion of the kink. Because the flow immediately beneath the reflected shock and between the two triple points is constant, this criterion is equivalent to requiring that the sonic line (in pseudo-stationary coordinates) intersect the kink. Also, the sonic line should have the same tangent at the kink as the second Mach stem, because the flow is supersonic ahead and subsonic behind this discontinuity. By using this criterion, the calculations show that the $M_s = 2.30$ case is a weak d.M.r. but that the cases where $1.70 \leqslant M_s \leqslant 2.20$ are c.M.rs, in reasonable agreement with figure 2. We remark that 45°, imperfect air calculations (not shown) are in somewhat better agreement.

Another sequence of cases for perfect argon with $M_s = 7.10$ has been calculated for various choices of θ_w with $49° \leqslant \theta_w \leqslant 54°$. The purpose of these calculations is to estimate the inviscid r.r. $\rightleftharpoons$ d.M.r. transition boundary and, by comparison with experimental results, to demonstrate and quantify the well known disagreement between theory and experiment for this issue (see, for example, Shirouzu & Glass 1982).

The experimental and computational double Mach-reflection configurations for $\theta_w = 49°$ are shown in figures 10*a*, *b*. These results are in substantial disagreement concerning the extent of the Mach stem region relative to the entire flow field. The computational results for $\theta_w = 53.2°$ are shown in figure 10*c*; this case is in much closer agreement with the experiment at $\theta_w = 49°$ than is figure 10*b*. The difference, $\Delta\theta_w \approx 4.0$–$4.5°$, may be viewed as the 'boundary-layer defect' (see Hornung & Taylor 1982; Shirouzu & Glass 1982; Wheeler & Glass 1985). We have attempted

to calculate the precise r.r. $\rightleftharpoons$ d.M.r. transition point by plotting the height of the Mach stem relative to h/L against θ_w for several computations in figure 10*d* and extrapolating the curve to zero height. The result is $\theta_w \approx 53.85°$, which disagrees moderately with the theoretical result of $\theta_w \approx 54.4°$ in Lee & Glass (1984). We remark that this error may be caused by an unnoticed bias in our measuring technique (done simply by using a ruler on the computer-generated contour plots of the blow-up Mach stem region), lack of numerical resolution when the Mach stem is only 1–2 zones high, or a numerical error in the post-shock flow field at the wall. In any case, the error is small relative to the viscous-inviscid difference and it is also possible that the theoretical inviscid prediction, which is an infinitesimal result, of $\theta_w \approx 54.4°$ does not apply when the entire disturbed flow field is taken into account.

6. Conclusions

A computer code has been developed for the inviscid, perfect gas shock-on-wedge problem and the results have been compared with the best available experimental data. The code is based on contemporary methodology and has only recently been available.

Good to excellent qualitative agreement has been obtained in all cases, and this applies to structures beneath the reflected shock such as the vortex roll-up as well as coarser criteria such as the reflection pattern. Non-equilibrium effects and viscous structures are the probable causes of the qualitative disagreements. Quantitatively, the results are very good for flow fields without observable non-equilibrium or viscous effects. When such effects are significant, errors of 10–15 % are typical. A pervasive but easily analysable numerical error present in most cases is the 'wall-heating' effect.

Although not entirely proven, it appears that the computer code represents a substantial predictive capability for the shock-on-wedge problem restricted to inviscid, perfect gases. Even for viscous, real gas flow fields, the computational results provide a significant amount of information, including highly resolved flow-field structures.

Significant non-equilibrium and viscous effects have been demonstrated in the shock-wave diffraction experiments. Much of this could be inferred without the numerical study, but the latter can provide a quantitative estimate of the various effects. In particular, vibrational relaxation is observed in the high shock-wave Mach number cases, and this can have large-scale effects on criteria such as the corner attachment angle and type (subsonic or supersonic) and viscous effects are important in determining the vortex roll-up pattern and the wedge corner flow field. Although these effects occur in thin layers or small regions, they may have an effect on the quantitative results in the inviscid portion of the flow field.

The capability of the computer code to discriminate between very small increments in problem parameters (M_s, θ_w, and the equation of state, although the latter has not been treated here) has been demonstrated.

By using parametrized sequences of calculations, it would be possible to construct transition boundaries in the (M_s, θ_w)-plane. Of course, the transitions obtained would be dependent on the transition criteria used in their construction;

our use of the sonic criterion in self-similar coordinates shows how the infinite amount of data potentially available from a calculation can be invaluable in evaluating one of the proposed criteria.

Also, we have been able to validate the conjecture that the r.r. $\rightleftharpoons$ d.M.r. transition is offset in experiments by a boundary-layer defect.

In future work, we intend to modify our computer code and include an approximation for vibrational relaxation. We expect that this work will settle some of the questions raised in this paper. The results presented here demonstrate, however, that a valid approximate solution method for the Navier–Stokes equations will be required if complete agreement between experiment and calculation is demanded. Despite these shortcomings, the comparison of the present numerical simulations with interferometric data from r.r., s.M.r., c.M.r. and d.M.r. experiments are probably the best available to date. Additional results are available in Glaz *et al.* (1985).

We are grateful to Mr Ralph Ferguson for his extensive programming work for these calculations. The discussions with Dr George Ullrich and Dr Allen Kuhl are very much appreciated.

The financial assistance received from the U.S. Department of Energy at the Lawrence Berkeley Laboratory under Contract DE-AC03-78SF00098; from the U.S. Defense Nuclear Agency under DNA Task Code Y99QAXSG and DNA Contract 001 83-C-0266; from the Naval Surface Weapons Center Independent Research Fund; from the U.S. Air Force Office of Scientific Research under Grant 82-0096; and from the Natural Science and Engineering Research Council of Canada is acknowledged with thanks.

References

Ando, S. & Glass, I. I. 1981 *Proc. 7th Int. Symp. on the Military Applications of Blast Simulation* Alberta, Canada: Defence Research Establishment.

Ben-Dor, G. & Glass, I. I. 1978 *AIAA Jl* **16**, 1146.

Ben-Dor, G. & Glass, I. I. 1979 *J. Fluid Mech.* **92**, 459–496.

Ben-Dor, G. & Glass, I. I. 1980 *J. Fluid Mech.* **96**, 735–756.

Boyer, A. G. 1964 *University of Toronto, UTIAS Report no.* 99.

Colella, P. & Glaz, H. H. 1982 *Proc. 8th Int. Conf. on Numerical Methods in Fluid Dynamics, Aachen* (ed. E. Krause). Berlin: Springer-Verlag.

Colella, P. & Glaz, H. M. 1983 *Lawrence Berkeley Laboratory Report* LBL-15776.

Colella, P. & Glaz, H. M. 1985 *J. Comput. Phys.* (In the press.)

Colella, P. & Woodward, P. R. 1984 *J. Comput. Phys.* **54**, 174–201.

Deschambault, R. L. & Glass, I. I. 1983 *J. Fluid Mech.* **131**, 27–57.

Deschambault, R. L. 1984 *University of Toronto, UTIAS Report no.* 270.

Glaz, H. M., Colella, P., Glass, I. I. & Deschambault, R. L. 1985 *UTIAS Report no.* 285.

Hall, J. G. 1954 *University of Toronto, UTIAS Report no.* 27.

Hansen, C. F. 1959 NASA TRR-50.

Hornung, H. G. & Taylor, J. R. 1982 *J. Fluid Mech.* **123**, 143–153.

Hu, J. T. C. 1985 *UTIAS TN no.* 253.

Hu, J. T. C. & Glass, I. I. 1985 (Submitted.)

Hu, J. T. C. & Shirouzu, M. 1985 *UTIAS Report no.* 283.

Jones, D. H., Martin, P. M. E. & Thornhill, C. K. 1951 *Proc. R. Soc. Lond.* A **209**, 238–247.

Lee, J.-H. & Glass, I. I. 1982 *University of Toronto, UTIAS Report no.* 262.

Lee, J.-H. & Glass, I. I. 1984 *Prog. aerospace Sci.* **21**, 33–80.
Li, J.-C. & Glass, I. I. 1985 *University of Toronto, UTIAS Report no.* 290.
Mach, E. 1878 *Akad. Wiss. Wien*, **77**, 819–838.
von Neumann, J. 1943 *Explosives Research Report no.* 12. Washington D.C.: Navy Dept. Bureau of Ordnance.
Noh, W. F. 1976 *Lawrence Livermore National Laboratory Report* UCRL-52112.
Shirouzu, M. & Glass, I. I. 1982 *University of Toronto, UTIAS Report, no.* 264.
Wheeler, J. 1985 *UTIAS Tech. Note no.* 256.
Wheeler, J. & Glass, I. I. 1985 (In preparation.)